Chemical Science

ROYAL SOCIETY OF CHEMISTRY

EDGE ARTICLE

View Article Online
View Journal | View Issue

Cite this: *Chem. Sci.*, 2024, **15**, 3730

All publication charges for this article have been paid for by the Royal Society of Chemistry

Received 27th November 2023
Accepted 31st January 2024

DOI: 10.1039/d3sc06347j

rsc.li/chemical-science

Stabilizing a $Li_{1.3}Al_{0.3}Ti_{1.7}(PO_4)_3$/Li metal anode interface in solid-state batteries with a LiF/Cu-rich multifunctional interlayer†

Decheng Ding,[ab] Hui Ma,[c] Huachao Tao, *[be] Xuelin Yang *[b] and Li-Zhen Fan *[d]

$Li_{1.3}Al_{0.3}Ti_{1.7}(PO_4)_3$ (LATP) has attracted much attention due to its high ionic conductivity, good air stability and low cost. However, the practical application of LATP in all-solid-state lithium batteries faces serious challenges, such as high incompatibility with lithium metal and high interfacial impedance. Herein, a CuF_2 composite layer was constructed at a Li/LATP interface by a simple drop coating method. CuF_2 in the interlayer reacts with lithium metal *in situ* to form a multifunctional interface rich in Cu and LiF. The multifunctional layer not only brings about close interfacial contact between LATP and Li metal, but also effectively prevents the electrochemical reaction of LATP with Li metal, and suppresses the electron tunneling and dendrite growth at the interface. The interfacial resistance of Li/CuF_2@LATP/Li symmetric batteries is significantly reduced from 562 to 92 Ω, and the critical current density is increased to 1.7 mA cm^{-2}. An impressive stable cycle performance of over 6000 h at 0.1 mA cm^{-2}/0.1 mA h cm^{-2}, 2200 h at 0.2 mA cm^{-2}/0.2 mA h cm^{-2} and 1600 h at 0.3 mA cm^{-2}/0.3 mA h cm^{-2} is achieved. Full batteries of $LiFePO_4$/CuF_2@LATP/Li also show a high capacity retention ratio of 80.3% after 540 cycles at 25 °C. This work provides an effective and simple composite layer solution to address the interfacial problem of Li/LATP.

1. Introduction

In recent decades, lithium-ion batteries have been widely used in our daily life, including transportation, portable electronic products, large-scale energy storage, military equipment, *etc.*[1–4] However, to meet the increasing demand for ultra-high energy density, traditional lithium-ion batteries face great challenges.[5] Lithium metal is considered as an ideal anode because of its very high theoretical specific capacity (3.86 A h g^{-1}) and the lowest reduction potential (−3.05 V).[6,7] However, lithium dendrite formation and its side reactions with organic electrolytes have seriously hindered the development and commercial application of liquid lithium metal batteries.[8] Solid-state batteries that use solid-state electrolytes (SSEs) instead of liquid electrolytes are considered to be the ultimate solution to solve the above problems.[9–11] As a typical sodium superionic conductor (NASICON) type oxide SSE, $Li_{1.3}Al_{0.3}Ti_{1.7}(PO_4)_3$ (LATP) has the advantages of high ionic conductivity (10^{-4} to 10^{-3} S cm^{-1}) at room temperature, a wide electrochemical window (>5 V), excellent moisture resistance and air stability, simple preparation and low cost.[12–14] However, there are two key problems that prevent the application of LATP. Firstly, solid–solid point contact at the electrode and electrolyte interface results in high interfacial impedance. Secondly, LATP is thermodynamically unstable against lithium metal. Side reactions at the interface of Li/LATP occur after direct contact, and Ti^{4+} spontaneously reduces to a lower valence state.[15–17] The side reaction results in the formation of a mixed conductive interface layer including a high electron conductivity phase, which makes the reaction further develop inwards, and the dendrites grow rapidly through the electrolyte.[18] In addition, the high stress concentration between the expanded decomposition region and the unreacted region leads to the formation and propagation of cracks. This leads to a sharp increase in interfacial impedance and is also the main cause of battery failure.[19,20] Based on the above problems, it is extremely urgent to build a stable and reliable intermediate layer at the Li/LATP interface.

In order to overcome the above challenges, the introduction of an artificial interface layer is considered to be one of the most effective solutions. A large number of reported Li/LATP interfacial modification strategies can be divided into inorganic layers, organic layers and composite layers.[21] The inorganic

[a]College of Electrical Engineering & New Energy, China Three Gorges University, Yichang, Hubei 443002, China

[b]College of Materials and Chemical Engineering, Hubei Provincial Collaborative Innovation Center for New Energy Microgrid, China Three Gorges University, Yichang, Hubei 443002, China. E-mail: huachaotao@ctgu.edu.cn; xlyang@ctgu.edu.cn

[c]Hubei Three Gorges Polytechnic, Yichang, Hubei 443000, China

[d]Beijing Advanced Innovation Center for Materials Genome Engineering, Institute of Advanced Materials and Technology, University of Science and Technology Beijing, Beijing 100083, China. E-mail: fanlizhen@ustb.edu.cn

[e]Hubei Three Gorges Laboratory, Yichang, Hubei 443007, China

† Electronic supplementary information (ESI) available. See DOI: https://doi.org/10.1039/d3sc06347j

layers contain metals (Ge and Al),[20,22,23] metal oxides (Al_2O_3, ZnO, and SnO_2), [16,24,25] halides (ZnF_2 and AgI),[26,27] among others. These inorganic layers can effectively protect LATP and enhance lithium wettability. Moreover, *in situ* reactions of these inorganic layers with Li anode can form alloy, LiF, Li_3N and other excellent interfacial components. But the interface is still a solid–solid contact, and it is difficult for the inorganic layer to improve the utilization ratio of lithium metal during the charge and discharge process in long-term cycling. And the methods of introducing coatings such as chemical vapor deposition (CVD), magnetron sputtering (MS), atomic layer deposition (ALD), *etc.* require specific equipment. For organic layers, poly(ethylene oxide)/$LiClO_4$,[28–30] poly(ethylene glycol) methyl ether acrylate,[31] polyvinylidene fluoride-hexafluoropropylene (PVDF-HFP)/LiTFSI,[32] and PVDF-TrFE[33] layers have been widely investigated. The flexible organic layers provide good interfacial contact, but high temperature dependence, poor mechanical properties, and short cycle life limit their practical use. Regarding the organic–inorganic composite layer, the current work includes a BN film,[34] $BaTiO_3$/P[VDF-TrFE-CTFE],[35] LiF/PVDF-HFP,[36] Mg_3N_2/PVDF,[37] Kevlar aramid nanofiber membrane,[38] *etc.* As a simple and low-cost modification strategy, the composite layer can combine the advantages of inorganic and organic layers to achieve a better balance in terms of effective Li/LATP isolation, low interfacial impedance and dendrite inhibition.

Herein, we propose a strategy for rapidly forming a CuF_2 composite layer on the LATP surface using the drop coating method. As shown in Fig. 1a, due to the poor interfacial contact and severe spontaneous reaction of the Li/LATP interface, an inhomogeneous-interface phase is formed. Stress concentration occurs between the expanded reactive phase and the unreactive phase, resulting in continuous crack evolution and rapid dendrite growth. In contrast, through the introduction of the CuF_2 composite layer at the Li/LATP interface, the electrochemical performance has been significantly improved. The *in situ* reaction between CuF_2 and lithium metal has formed a multifunctional flexible interlayer rich in Cu and LiF. [39,40] The multifunctional interlayer provides a dynamic, compact contact that is adaptable to volume changes, effectively avoids interfacial side reactions between Li metal and LATP, eliminates stress concentration and cracks, and also suppresses dendrite growth to achieve uniform lithium deposition (Fig. 1b). The interfacial resistance of the Li/CuF_2@LATP/Li symmetric batteries is reduced by an order of magnitude. The Li/CuF_2@LATP/Li symmetric batteries also exhibit a high critical current density of 1.7 mA cm^{-2}. Long-term stable cycles of over 6000 h at 0.1 mA cm^{-2}/0.1 mA h cm^{-2}, 2200 h at 0.2 mA cm^{-2}/0.2 mA h cm^{-2} and 1600 h at 0.3 mA cm^{-2}/0.3 mA h cm^{-2} can be achieved. The Li/CuF_2@LATP/$LiFePO_4$ full batteries can be stably charged and discharged for 540 and 100 cycles at 0.5C and 0.2C under 25 °C, and the corresponding capacity retention ratios are 80.3% and 93.5%, respectively.

2. Results and discussion

$Li_{1.3}Al_{0.3}Ti_{1.7}(PO_4)_3$ (LATP) was synthesized by a traditional solid-state sintering method. The X-ray diffraction (XRD) patterns of LATP pellets are well matched with the standard peaks of rhomboid NASICON $LiTi_2(PO_4)_3$ (PDF# 35-0754) (Fig. S1a†). Scanning electron microscopy (SEM) shows that LATP pellets have a very dense morphology (Fig. S1b and c†), which confirms their high relative density (about 95%). The ionic conductivity of LATP pellets measured by electrochemical impedance spectroscopy (EIS) is 4.9×10^{-4} S cm^{-1} at 25 °C (Fig. S1d†). A temperature dependence test shows that LATP pellets have a lower activation energy of 0.32 eV (Fig. S1e and f†).

A simple and rapid drop coating method was used to introduce the multifunctional interface layer. 20 μL of CuF_2 mixed solution containing different mass ratios was dropped onto the LATP pellets, and a uniform blue coating was obtained after drying (Fig. S2†). The detailed steps are shown in the experimental section. The contact angle of DME with LATP pellets is almost zero, indicating its better wettability compared with common solvents, which is beneficial to form a uniform coating (Fig. S3†). Compared with the original LATP pellets, the surface of the modified LATP pellets is more compact and uniform, and the flexible coating can fill the pore defects on the LATP surface and provide good interfacial contact (Fig. 2a–c). Further observation of the cross-section morphology shows that the coating is uniformly covered on the LATP surface with a thickness of about 15 μm, and the contact between the coating and the LATP is very close without obvious gaps (Fig. 2d–f). The EDS mapping images of the cross section display the uniform distribution and clear stratification of Ti, P, Al, F and Cu elements (Fig. 2g), further proving the successful introduction of a uniform CuF_2 composite layer.

A constant current charge–discharge test of the symmetric lithium battery was carried out at 25 °C to verify the influence of the multifunctional layer on the interfacial stability between Li metal and LATP. At 0.1 mA cm^{-2}/0.1 mA h cm^{-2}, the overpotential of the Li/LATP/Li symmetric battery continues to increase, and the battery soon fails (Fig. 3a). This can be attributed to the formation of a non-uniform-interface phase and the continuous evolution of stress cracks after the reaction of LATP and Li, which reduces the Li^+ diffusion coefficient and results in high concentration polarization. The voltage–time curves of the symmetric batteries assembled using LATP with 5 wt%, 10 wt% and 15 wt% CuF_2 are shown in Fig. S4.† The symmetric batteries with different concentrations of CuF_2 show a longer cycle life and more stable trend. Among them, the Li/10 wt% CuF_2@LATP/Li symmetric battery shows the best electrochemical performance. Moreover, CuF_2 layers with different thicknesses were prepared by varying the amount of 10 wt% CuF_2 solution (10 μL, 20 μL and 30 μL). The effect of CuF_2 layers with different thicknesses on the electrochemical performance of the symmetrical battery was further investigated (Fig. S5†). The symmetrical battery with the 15 μm CuF_2 layer has a moderate polarization voltage, flat voltage platform and the most stable cycling performance. The pure physical barrier has little improvement on interfacial stability. The symmetrical battery with the 7 μm CuF_2 layer exhibits a large initial polarization voltage of 72 mV and a steep voltage plateau, and completely short-circuits after 250 h, which may be caused by the uneven interface. The symmetrical battery with the 32 μm

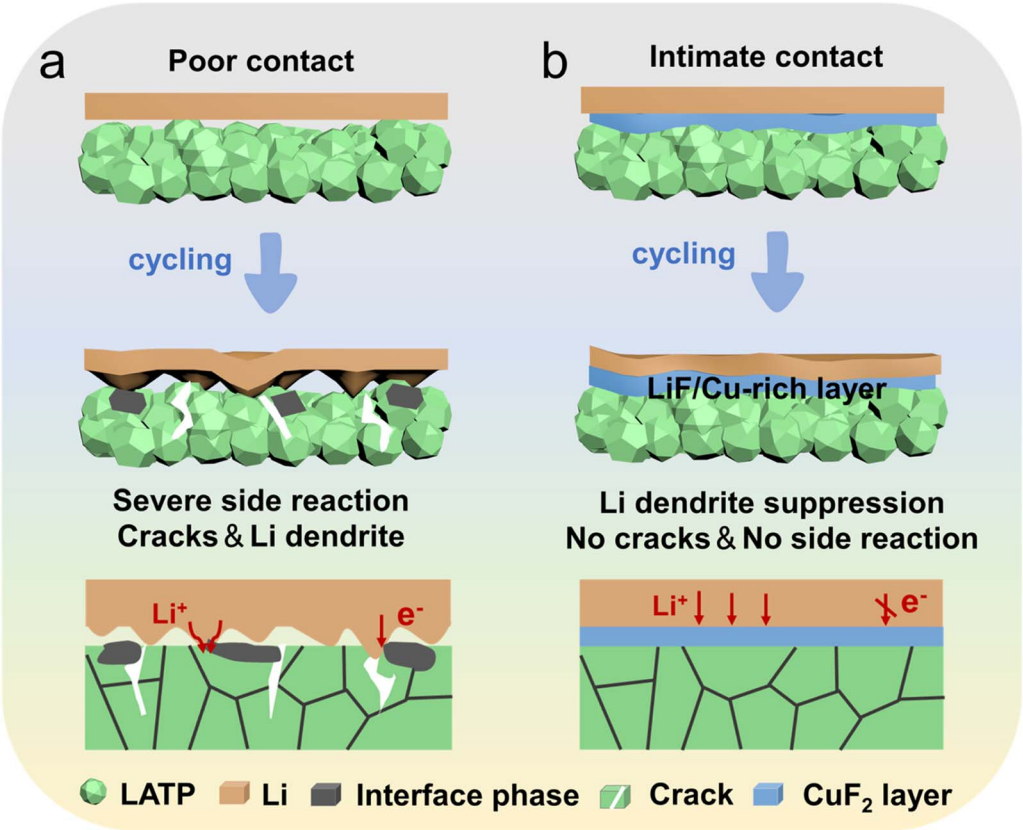

Fig. 1 Interface evolution of (a) Li/LATP and (b) Li/CuF_2@LATP interfaces.

CuF_2 layer has a maximum polarization voltage of 116 mV and short circuits after 210 h. A too thick CuF_2 layer may hinder the fast diffusion of Li^+ between layers. For convenience, 10 wt% CuF_2 with a volume of 20 μL is employed during the subsequent test and named CuF_2. Specifically, the Li/CuF_2@LATP/Li symmetric battery delivers an outstanding long cycle performance of 6000 h, a lower voltage overpotential of around 40 mV and no unilateral polarization. Fig. 3b shows the voltage–time curves of four different cycle periods, all of which show a symmetrical flat polarization voltage platform with no concentration polarization. Even after 4000 h of cycling, the polarization voltage does not significantly change. This is in sharp contrast to the rising polarization voltage and high concentration polarization of bare LATP, indicating that the interface maintains a dynamic close contact after the CuF_2 composite layer modification, showing good ion transport dynamics. After cycling at a higher current density of 0.2 mA cm^{-2} (Fig. 3c) or 0.3 mA cm^{-2} (Fig. S6†), the Li/CuF_2@LATP/Li symmetrical batteries still show good cycling performance and could stably cycle for more than 2200 h and 1600 h, and keep low polarization overpotentials of about 60 and 80 mV. Even at a high current density of 0.5 mA cm^{-2} and fixed capacity of 0.5 mA h cm^{-2}, Li/CuF_2@LATP/Li can cycle stably for more than 250 h (Fig. S7†). However, the Li/LATP/Li symmetric battery under the same conditions cannot operate normally (Fig. S8†). Furthermore, in order to investigate the effect of CuF_2 on the electrochemical performance of symmetric batteries, symmetrical batteries were assembled with PVDF/LiTFSI/$LiNO_3$ coated LATP pellets (PVDF@LATP). The Li/PVDF@LATP/Li symmetric battery is very unstable at 0.1 mA cm^{-2}/0.1 mA h cm^{-2}, and the polarization voltage is about 136 mV (Fig. S9†). This result further indicates that the interlayer without CuF_2 is difficult to stabilize the LATP/Li interface at 25 °C.

Electrochemical impedance spectroscopy (EIS) was performed to further study the effect of the CuF_2 layer on the dynamic behavior of the Li/LATP interface. The impedances of the Li/LATP/Li and Li/CuF_2@LATP/Li symmetric batteries before cycling (Fig. 3d) and after different cycling times (Fig. S10†) were compared and fitted using an equivalent circuit model (Fig. S11†). The semi-circle in the high frequency region corresponds to the grain boundary resistance R_{gb}, and the semi-circle in the low frequency region corresponds to the interfacial resistance R_{int} between the Li metal anode and the electrolyte. Fig. 3e shows the interfacial impedance variations of the Li/LATP/Li and Li/CuF_2@LATP/Li symmetric batteries before cycling and after cycling for 100, 200 and 400 h. The interfacial resistances R_{int} of the Li/LATP/Li symmetric battery are 562 Ω before cycling, and 1006 Ω, 2931 Ω, and 4083 Ω after 100, 200 and 400 h cycles, respectively. The sharp increase in interfacial resistance during cycles indicates a serious deterioration of the Li/LATP interface, which corresponds to the continuous increase in the overpotential of the Li/LATP/Li symmetric battery during the charge and discharge process. In contrast,

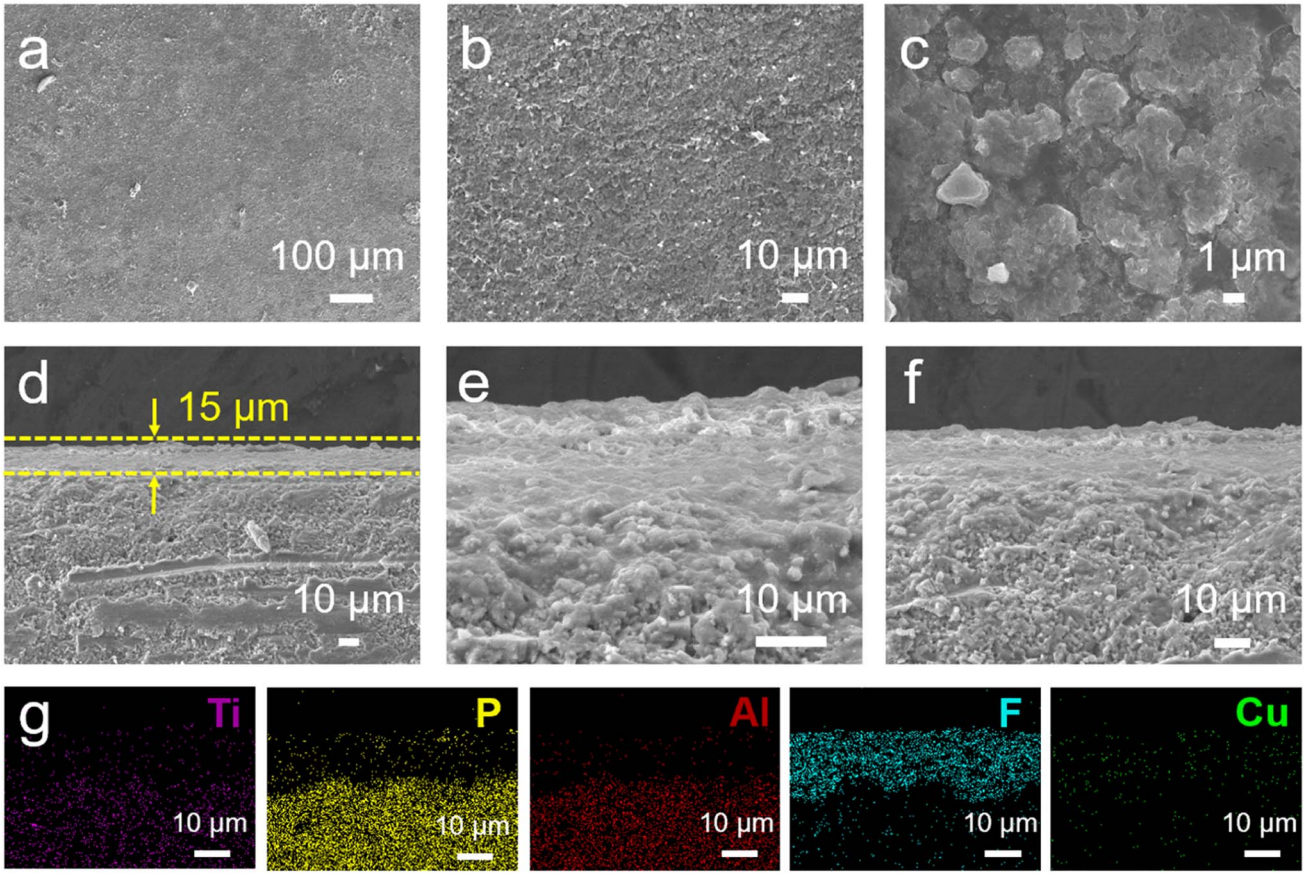

Fig. 2 (a–c) Surface and (d–f) cross-section SEM images of a CuF_2@LATP pellet. (g) Corresponding EDS mapping images of CuF_2@LATP.

the R_{int} of Li/CuF_2@LATP/Li before cycling is reduced to 92 Ω, indicating a tight interfacial contact. After cycling for 100, 200 and 400 h, the values of R_{int} are 98 Ω, 105 Ω and 108 Ω, respectively, with little change. The stable interfacial resistance during cycles indicates that the interfacial stability of Li/CuF_2@LATP is significantly improved. The introduction of a CuF_2 composite layer effectively reduces the interfacial resistance and improves the electrochemical stability.

To further demonstrate the electrochemical stability of the Li/CuF_2@LATP interface and the ability to inhibit Li dendrite penetration, critical current density (CCD) measurements were performed. A higher CCD represents a stronger dendrite suppression capability.[41] The CCD of the symmetric battery was measured under time-constant mode, in a fixed cycling period, and the areal capacity of Li plating or striping gradually increases (1 h per half-cycle). When the current density rises to 0.2 mA cm^{-2}, the voltage polarization of the Li/LATP/Li symmetric battery increases and then suddenly decreases, indicating the formation of Li dendrites and the occurrence of a partial short circuit in LATP. In contrast, Li/CuF_2@LATP/Li symmetric batteries exhibit no short circuit and sudden voltage drop even at 1.7 mA cm^{-2} (Fig. 3f), indicating a great improvement in suppressing lithium dendrites. The rate performance of the Li/CuF_2@LATP/Li symmetric battery was also tested (Fig. 3g). When the testing conditions are 0.05/0.05, 0.1/0.1, 0.2/0.2, 0.3/0.3, 0.4/0.4, 0.5/0.5 and 0.6/0.6 mA cm^{-2}/mA h cm^{-2}, the overpotentials of Li/CuF_2@LATP/Li symmetric batteries are 21, 39, 66, 78, 86, 106, 126 and 159 mV, respectively. After restoration to 0.1/0.1 mA cm^{-2}/mA h cm^{-2}, the overpotential can return to the previous value (about 38 mV), indicating the good robustness of the CuF_2@LATP interface. The electrochemical performance comparison of other interfacial modifications for NASICON-type oxide solid electrolyte in lithium batteries with this work is displayed in Fig. 3h.[42,43] The CuF_2 composite layer exhibits remarkable cycle stability.

After 100 cycles at 0.1 mA cm^{-2}, the original LATP pellets are completely broken, while the CuF_2@LATP pellets remain intact (Fig. S12†). After removing the lithium metal anode and coating, the micromorphology of LATP pellets was further observed by SEM. The surface of LATP is severely eroded and shows obvious cracks after cycling (Fig. 4a and c), confirming the occurrence of severe side reactions at the interface of Li/LATP caused by the uneven electric field and physical contact and the formation of by-products and stress cracks. In contrast, CuF_2@LATP shows better integrity and no cracks appear on the surface after 100 cycles (Fig. 4e and g). It is proved that the CuF_2 composite layer can suppress the side reaction between LATP and the Li anode, preventing the erosion of electrolyte by Li. In cross-sectional SEM images, a thicker interface phase generated by side reactions can be observed at the Li/LATP interface, which damages

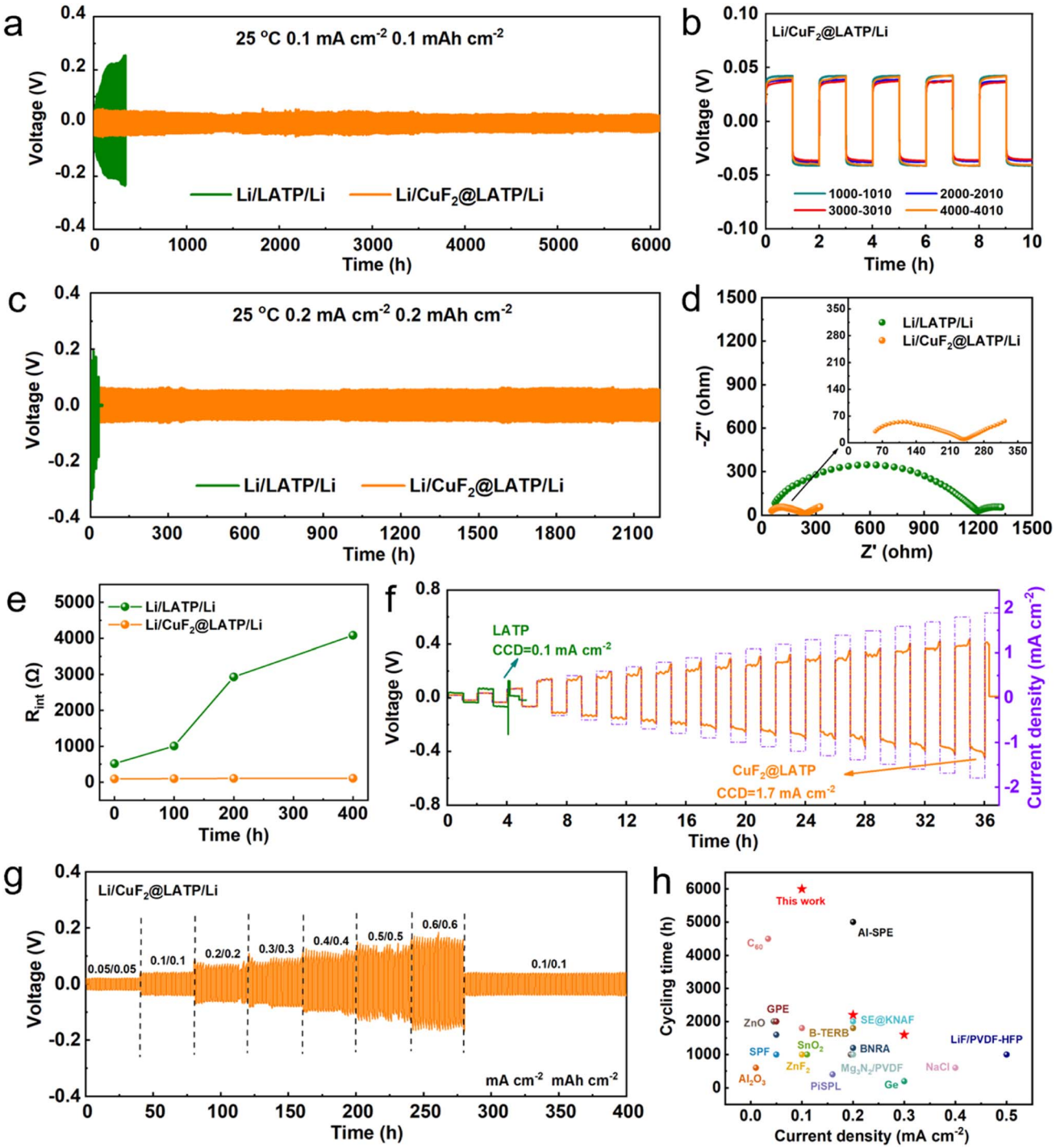

Fig. 3 (a) Voltage–time curves of Li/LATP/Li and Li/CuF_2@LATP/Li symmetrical batteries at 0.1 mA cm^{-2}/0.1 mA h cm^{-2}. (b) The magnified voltage–time curves of Li/CuF_2@LATP/Li under specific cycle times. (c) Voltage–time curves of Li/LATP/Li and Li/CuF_2@LATP/Li symmetrical batteries at 0.2 mA cm^{-2}/0.2 mA h cm^{-2}. (d) EIS curves of Li/LATP/Li and Li/CuF_2@LATP/Li symmetric batteries before cycling. (e) The interfacial resistance changes of Li/LATP/Li and Li/CuF_2@LATP/Li symmetric batteries after different cycle times at 0.1 mA cm^{-2}/0.1 mA h cm^{-2}. (f) Voltage–time curves of Li/LATP/Li and Li/CuF_2@LATP/Li symmetric batteries under progressively increasing current density. (g) Rate performance of Li/CuF_2@LATP/Li symmetric batteries at 25 °C. (h) The electrochemical performance comparison of NASICON-type oxide solid electrolyte with this work.

the originally dense structure (Fig. 4b and d). When LATP is in contact with Li metal, Ti^{4+} will spontaneously reduce to a lower valence state, which results in the formation of an undesirable amorphous and volume expansion interface phase.[44] After 100 cycles, no reduction products or cracks can be detected, and the tightly stacked grains are similar to those before cycling in the

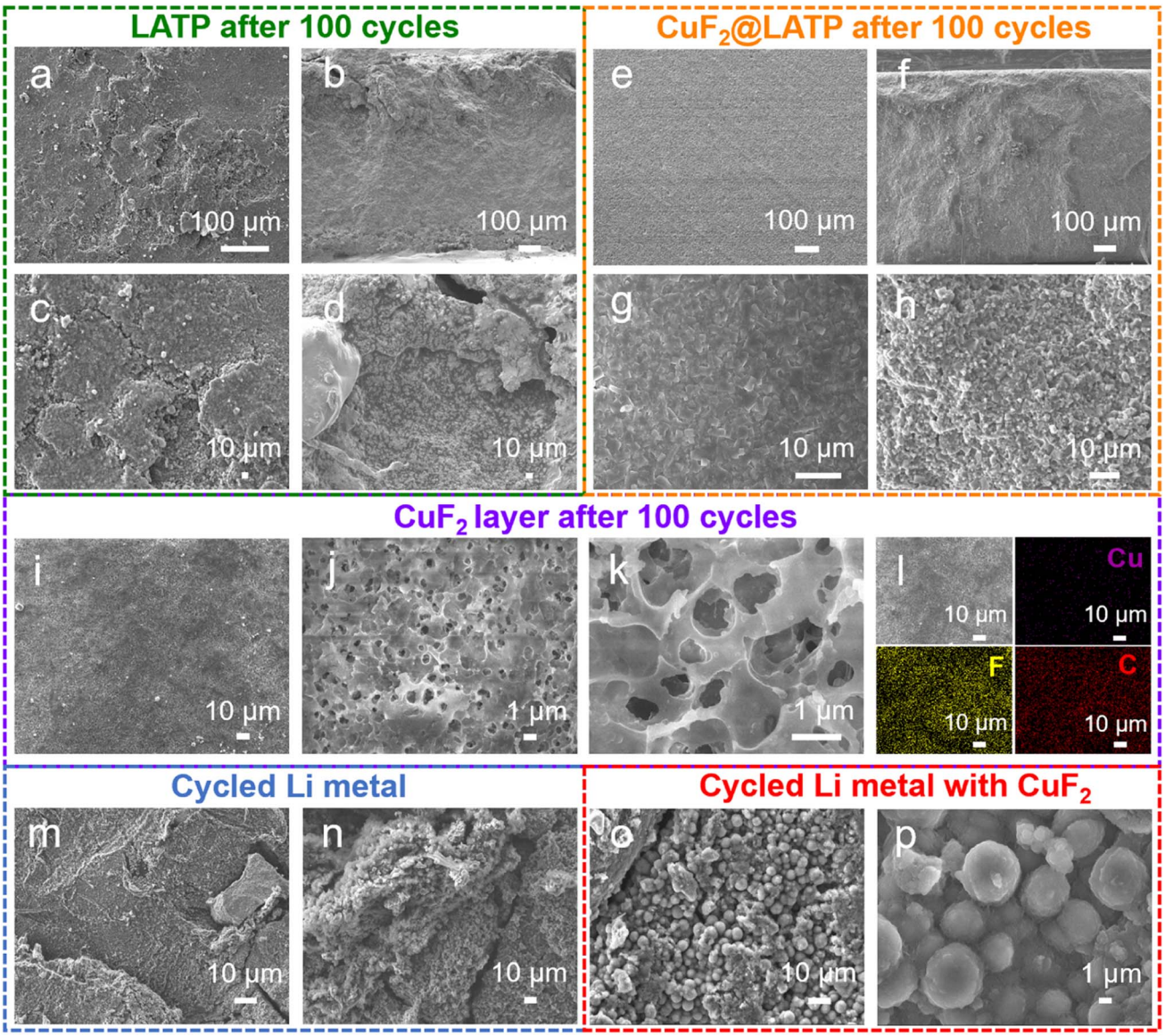

Fig. 4 (a and c) Surface and (b and d) cross-sectional SEM images of a LATP pellet after 100 cycles at 0.1 mA cm^{-2}/0.1 mA h cm^{-2}. (e and g) Surface and (f and h) cross-sectional SEM images of CuF_2@LATP after 100 cycles at 0.1 mA cm^{-2}/0.1 mA h cm^{-2}. (i–k) Surface SEM and (l) corresponding EDS mapping images of the CuF_2 layer after 100 cycles. Surface SEM images of lithium metal anodes in the (m and n) Li/LATP/Li and (o and p) Li/CuF_2@LATP/Li symmetric batteries after 100 cycles at 0.1 mA cm^{-2}/0.1 mA h cm^{-2}.

cross-section of CuF_2@LATP, indicating that no obvious side reaction occurs (Fig. 4f and h). In addition, the microstructure of the CuF_2 layer after cycling was further characterized. The surface of the CuF_2 layer after cycles shows uniform, continuous, and porous polymer characteristics without obvious cracks (Fig. 4i–l). EDS mapping images exhibit the uniform distribution of Cu, F and C elements, indicating the uniform distribution of Cu and LiF on the PVDF matrix (Fig. S13 and S14†). In the cross-section SEM image, the interlayer also shows a complete structure after cycles and is tightly coated on the LATP pellet (Fig. S14†). This result indicates that the CuF_2 composite layer can maintain good integrity after long cycles. The surface morphologies of Li metal anodes after 100 cycles were also explored. A large amount of lithium dendrites and lithium powder appear on the surface of the lithium metal anode in the Li/LATP/Li symmetric battery after 100 cycles (Fig. 4m and n). In contrast, in the Li/CuF_2@LATP/Li symmetric battery, the surface of the lithium metal anode after 100 cycles is a more uniform spherical deposit of lithium (Fig. 4o and p). The formed LiF/Cu-rich multifunctional layer provides multiple nucleation sites, which effectively constrain the nucleation and growth of lithium, resulting in the isotropic spherical characteristics of plated Li. The spherical lithium deposition guided by the lithiophilic interface layer can greatly reduce the side reaction of the interface, avoid the formation of dead lithium, and effectively improve the utilization rate of the lithium anode.[45] These results indicate that the introduction of a CuF_2 composite layer can inhibit dendrite growth and guide uniform Li

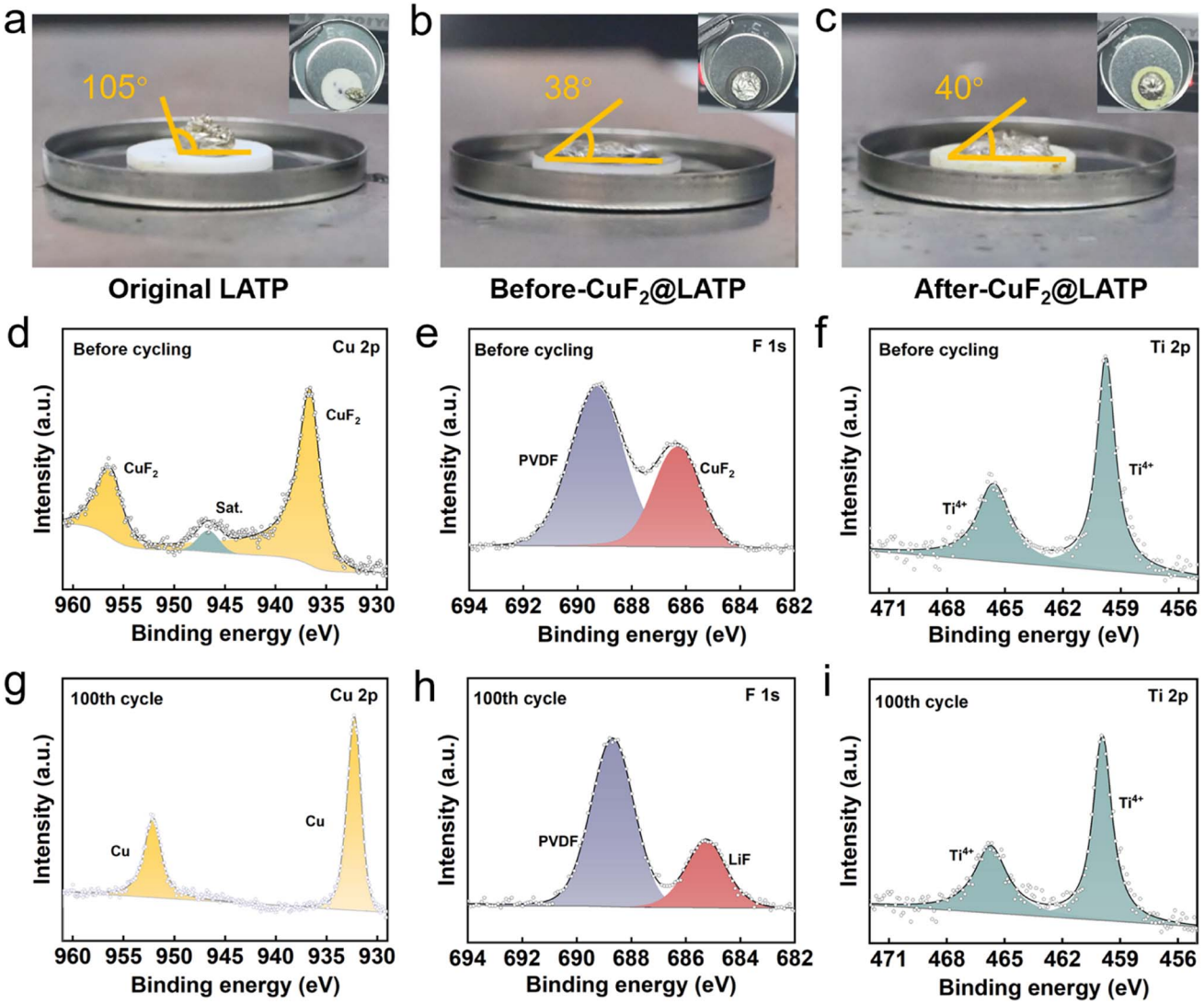

Fig. 5 The contact angle tests of molten lithium with (a) LATP pellets, (b) CuF_2@LATP pellets before cycling and (c) CuF_2@LATP pellets after 100 cycles. High-resolution (d and g) Cu 2p, (e and h) F 1s and (f and i) Ti 2p XPS spectra of the CuF_2@LATP surface (d–f) before cycling and (g–i) after 100 cycles.

deposition, verifying the enhanced chemical/electrochemical stability of the Li/CuF_2@LATP interface.

The electronic conductivity of LATP is also one of the important factors for inhibiting dendrite growth.[46,47] The CuF_2@LATP pellets before and after the reduction reaction of CuF_2 and Li metal are named before-CuF_2@LATP and after-CuF_2@LATP, respectively. The electronic conductivities of before-CuF_2@LATP and after-CuF_2@LATP are 1.10×10^{-10} and 3.14×10^{-10} S cm^{-1}, indicating the slight increase of electronic conductivity from before the reduction reaction to after the reduction reaction, which are two orders of magnitude lower than that of Ag/LATP/Ag (1.11×10^{-8} S cm^{-1}) (Fig. S15†). Although the interfacial reaction product Cu component has high electronic conductivity, LiF with insulating characteristics plays a dominant role in the inhibition of electronic conduction.[48] Therefore, after-CuF_2@LATP has a lower electron conduction capacity than the original LATP, which can effectively block electron tunneling at the interface, avoid side reactions and suppress dendrite growth. Moreover, the Cu component in the interlayer can improve the uneven electric field distribution, effectively reduce the interfacial resistance and guide uniform Li deposition. The LiF/Cu-rich multifunctional layer not only protects LATP by preventing electron injection, but also achieves the effect of reducing interfacial resistance similar to the mixed ion electron conduction layer.

In order to confirm the enhanced lithiophilicity by the CuF_2 interlayer, the contact angles of molten lithium with original LATP and CuF_2@LATP before and after the reduction reaction are further measured. The contact angle between molten lithium and the original LATP pellet is about 105°, and molten lithium is easily separated after tilting (Fig. 5a). In contrast, molten lithium shows good wettability on both CuF_2@LATP pellets before and after the reduction reaction, possessing small contact angles of about 38° and 40°, respectively (Fig. 5b and c).

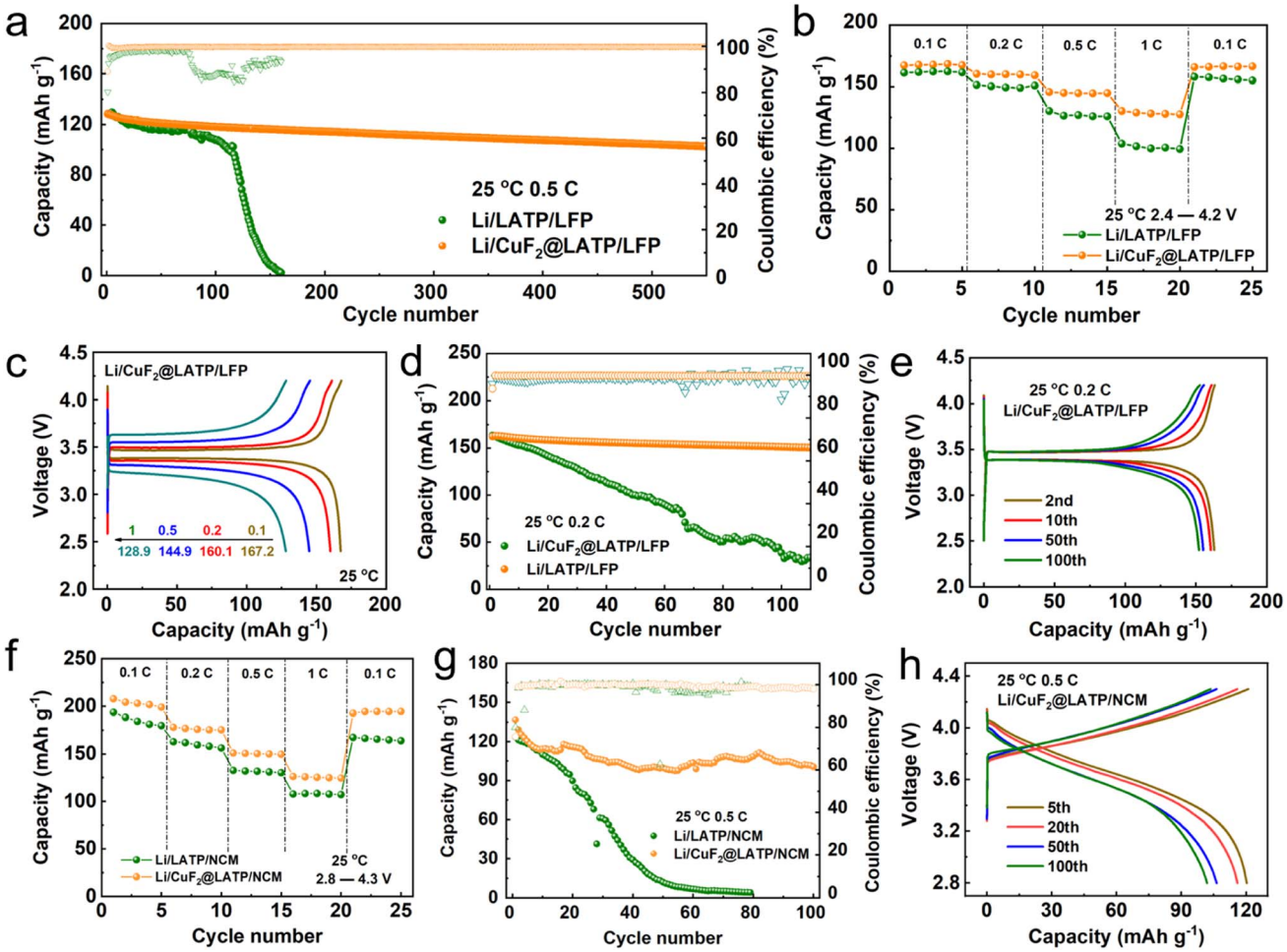

Fig. 6 (a) Cycle performance of the Li/CuF_2@LATP/LFP and Li/LATP/LFP full batteries at 25 °C and 0.5C. (b) Rate performance of the Li/CuF_2@LATP/LFP and Li/LATP/LFP full batteries. (c) Charge and discharge curves at different rates of Li/CuF_2@LATP/LFP. (d) Cycle performance of Li/CuF_2@LATP/LFP and Li/LATP/LFP at 0.2C. (e) Charge and discharge curves of Li/CuF_2@LATP/LFP at 0.2C under different cycles. (f) Rate performance of Li/CuF_2@LATP/NCM and Li/LATP/NCM. (g) Cycle performance of Li/CuF_2@LATP/NCM and Li/LATP/NCM at 25 °C and 0.5C. (h) Charge and discharge curves of Li/CuF_2@LATP/NCM at 0.5C under different cycles.

Molten lithium tightly bonds with CuF_2@LATP pellets before and after the reduction reaction, indicating that the lithiophilicity of LATP pellets is significantly improved after the introduction of the CuF_2 interlayer. Moreover, the chemical and electrochemical reaction mechanism of CuF_2@LATP with the lithium metal anode was further studied using *ex situ* XPS. In the Cu 2p spectrum, the two main peaks of CuF_2@LATP before cycling at 956.3 eV and 936.5 eV are attributed to CuF_2 (Fig. 5d). After 100 cycles in the Li/CuF_2@LATP/Li symmetric battery, two peaks of the Cu 2p XPS spectrum at 952.2 and 932.2 eV correspond to the metallic Cu element (Fig. 5g). The two main peaks of F 1s XPS before cycling can be derived from PVDF and CuF_2 (Fig. 5e). After 100 cycles, a new peak of 685.1 eV appears in F 1s, corresponding to LiF (Fig. 5h). The results indicate the reaction of the CuF_2 composite layer with Li metal during cycles, forming a stable multifunctional layer rich in Cu and LiF components. The multifunctional layer not only acts as a physical isolation but also brings about good interfacial contact between Li metal and LATP. Near the lithium metal side, the *in situ* generated LiF/Cu has a strong adsorption force on the lithium metal like a rivet, which makes the lithium metal and the flexible intermediate layer maintain dynamic close contact in the long-term cycle. On the LATP side, the flexible interface can fill the original pores and defects on the electrolyte surface to avoid contact with solid points. Moreover, the Cu component in the interlayer has high lithiophilicity, which can improve the electric field distribution, reduce the interfacial resistance, and help the uniform Li deposition. Finally, the high surface energy, electronic insulation ability and high mechanical strength of LiF bring about uniform lithium flux, which can effectively inhibit the formation and growth of lithium dendrites. The main peak in the N 1s XPS spectrum corresponds to NO^{3-}, located at 408.1 eV (Fig. S16†), which comes from $LiNO_3$ co-solvent. After cycles, NO^{3-} is converted to N^{3-}, indicating the formation of Li_3N. Li_3N has a high ionic conductivity and plays an active role in interfacial lithium transport.[49] In addition, the valence change of Ti^{4+} indicates that LATP has a chemical reaction with Li. In the Ti 2p spectra of CuF_2@LATP before and after 100

cycles, the two main peaks at 465.5 and 459.7 eV correspond to Ti^{4+}, and no significant shift and no reduction of the valence state can be observed (Fig. 5f and i), indicating that LATP has no interfacial reaction with Li metal. To sum up, the introduction of a CuF_2 composite layer significantly improves the interfacial stability, avoids the reaction between LATP and Li metal during cycles, inhibits electron injection at the interface, and achieves uniform lithium deposition.

$LiFePO_4$ (LFP) and $LiNi_{0.8}Co_{0.1}Mn_{0.1}O_2$ (NCM) were used as cathodes to assemble full batteries to further verify the durability of the modified Li/LATP interface, as shown in Fig. S17.† At 25 °C and a current density of 0.5C, the capacity retention ratio of the Li/LATP/LFP full battery falls below 60.5% after 120 cycles, and then brings about rapid capacity decay as well as battery failure. However, the Li/CuF_2@LATP/LFP full battery shows excellent cycling performance, with a high capacity retention ratio of 80.3% even after 540 cycles (Fig. 6a). The rate capabilities further indicate that the discharge capacities of the Li/CuF_2@LATP/LFP full battery at 0.1, 0.2, 0.5 and 1C are 167.2, 160.1, 144.9 and 128.9 mA h g^{-1}, respectively (Fig. 6c), and a high discharge capacity of 166.3 mA h g^{-1} is recovered when the rate returns to 0.1C again. Under the same conditions, the discharge capacities of the Li/LATP/LFP full battery are 161.3, 150.3, 126.4 and 101.5 mA h g^{-1}, respectively (Fig. S18a†), and the capacity recovers to only 156.4 mA h g^{-1} when the rate returns to 0.1C (Fig. 6b). The Li/CuF_2@LATP/LFP full battery also shows stable cycling performance at a lower current density of 0.2C, with a high initial discharge capacity of 162 mA h g^{-1} and capacity retention ratio of 93.5% after 100 cycles. However, for the Li/LATP/LFP full battery under the same conditions, the capacity retention rate is only 23.3% after 100 cycles (Fig. 6d). It can also be seen from the charge and discharge curves with different cycles at 0.2C that the polarization voltage of Li/CuF_2@LATP/LFP barely changes after 100 cycles (Fig. 6e). However, the polarization voltage of Li/LATP/LFP keeps increasing during cycles (Fig. S18b†). Moreover, the Li/PVDF@LATP/LFP full battery without CuF_2 exhibits an initial discharge capacity of only 94.5 mA h g^{-1} at 0.5C and 25 °C, and the discharge capacity is close to 0 mA h g^{-1} after 80 cycles (Fig. S19†), indicating that CuF_2 in the interlayer plays a key role.

The EIS curves of Li/CuF_2@LATP/LFP and Li/LATP/LFP full batteries before and after 100 cycles are further compared (Fig. S20†), and the fitted equivalent circuit is shown in Fig. S21.† After 100 cycles, the total interfacial resistance of the Li/LATP/LFP full battery increases substantially from 826 Ω to 20 740 Ω. In contrast, the total interfacial resistance of the Li/CuF_2@-LATP/LFP full battery before cycling and after 100 cycles does not change much from 103 Ω to 175 Ω. The multifunctional layer can bring about good interfacial stability and interfacial ion transport dynamics in the full battery. Moreover, the rate capability and cycling performance of Li/CuF_2@LATP/NCM and Li/LATP/NCM full batteries are also compared. The Li/CuF_2@-LATP/NCM full battery displays higher reversible capacities at various current densities than the Li/LATP/NCM full battery (Fig. 6f). At 0.5C, the Li/CuF_2@LATP/NCM full battery also exhibits better cycling stability after 100 cycles than the Li/LATP/NCM full battery and stable charge–discharge curves (Fig. 6g and h). These results indicate that the introduction of the multifunction CuF_2 layer significantly improves the cycling performance and rate capability of the all-solid-state lithium battery.

3. Conclusion

In summary, a CuF_2 composite layer has been constructed on the surface of LATP by a simple drip coating method. The *in situ* reaction of CuF_2 with lithium metal forms a multifunctional flexible interlayer rich in Cu and LiF. The interlayer brings about close interfacial contact, effectively avoids interfacial side reactions between Li metal and LATP, and eliminates stress concentration and cracks. It also hinders electron injection at the interface, inhibits dendrite growth at the interface and inside, and realizes uniform lithium deposition. Thanks to the multifunctional intermediate layer, the CCD of the improved LATP is increased to 1.7 mA cm^{-2}. The interfacial resistance of the Li/CuF_2@LATP/Li symmetric battery is reduced from 562 Ω to 92 Ω, achieving long-term stability at 0.1 mA cm^{-2}/0.1 mA h cm^{-2} for 6000 h, 0.2 mA cm^{-2}/0.2 mA h cm^{-2} for 2200 h, and 0.3 mA cm^{-2}/0.3 mA h cm^{-2} for 1600 h. At the same time, the capacity retention of Li/CuF_2@LATP/LFP batteries is 80.3% and 93.5% after 540 and 100 stable charge and discharge cycles at 25 °C, 0.5C and 0.2C, respectively, and the coulombic efficiency is greater than 99.5%. This simple and fast composite coating strategy can effectively improve the critical issues of the LATP/Li interface, providing potential feasibility for high-performance solid-state batteries.

Data availability

Preparation and characterizations of samples, electrochemical tests of battery, and additional data are available in ESI.†

Author contributions

The manuscript was written through contributions of all authors. All authors have given approval to the final version of the manuscript.

Conflicts of interest

The authors declare no competing financial interest.

Acknowledgements

The authors acknowledge the support from the National Natural Science Foundation of China (22179071), and the National Key R&D Program of China (2022YFB3807700), the Hubei Natural Science Foundation for Distinguished Young Scholars (2023AFA089), the Hubei Natural Science Foundation Innovation Group Project (2022CFA020), and the Joint Funds of the Hubei Natural Science Foundation Innovation and Development (2022CFD034), and the Major Technological Innovation Project of Hubei Science and Technology Department (2019AAA164).

References

1 X. B. Cheng, R. Zhang, C. Z. Zhao and Q. Zhang, Toward safe lithium metal anode in rechargeable batteries: a review, *Chem. Rev.*, 2017, **117**, 10403–10473.
2 J. B. Goodenough and Y. Kim, Challenges for rechargeable Li batteries, *Chem. Mater.*, 2010, **22**, 587–603.
3 J. Wen, D. Zhao and C. Zhang, An overview of electricity powered vehicles: lithium-ion battery energy storage density and energy conversion efficiency, *Renew. Energy*, 2020, **162**, 1629–1648.
4 Q. Yang and C. Li, Li metal batteries and solid state batteries benefiting from halogen-based strategies, *Energy Storage Mater.*, 2018, **14**, 100–117.
5 M. J. Lee, J. Han, K. Lee, Y. J. Lee, B. G. Kim, K. N. Jung, B. J. Kim and S. W. Lee, Elastomeric electrolytes for high-energy solid-state lithium batteries, *Nature*, 2022, **601**, 217–222.
6 A. Manthiram, S. H. Chung and C. Zu, Lithium-sulfur batteries: progress and prospects, *Adv. Mater.*, 2015, **27**, 1980–2006.
7 M. D. Tikekar, S. Choudhury, Z. Tu and L. A. Archer, Design principles for electrolytes and interfaces for stable lithium-metal batteries, *Nat. Energy*, 2016, **1**, 16114.
8 Z. Zhang, Y. Shao, B. Lotsch, Y. S. Hu, H. Li, J. Janek, L. F. Nazar, C. W. Nan, J. Maier, M. Armand and L. Chen, New horizons for inorganic solid state ion conductors, *Energy Environ. Sci.*, 2018, **11**, 1945–1976.
9 A. Manthiram, X. Yu and S. Wang, Lithium battery chemistries enabled by solid-state electrolytes, *Nat. Rev. Mater.*, 2017, **2**, 16103.
10 C. Sun, J. Liu, Y. Gong, D. P. Wilkinson and J. Zhang, Recent advances in all-solid-state rechargeable lithium batteries, *Nano Energy*, 2017, **33**, 363–386.
11 X. Miao, H. Wang, R. Sun, C. Wang, Z. Zhang, Z. Li and L. Yin, Interface engineering of inorganic solid-state electrolytes for high-performance lithium metal batteries, *Energy Environ. Sci.*, 2020, **13**, 3780–3822.
12 C. Niu, D. Liu, J. A. Lochala, C. S. Anderson, X. Cao, M. E. Gross, W. Xu, J. G. Zhang, M. S. Whittingham, J. Xiao and J. Liu, Balancing interfacial reactions to achieve long cycle life in high-energy lithium metal batteries, *Nat. Energy*, 2021, **6**, 723–732.
13 Q. Xu, C. L. Tsai, D. Song, S. Basak, H. Kungl, H. Tempel, F. Hausen, S. Yu and R. A. Eichel, Insights into the reactive sintering and separated specific grain/grain boundary conductivities of $Li_{1.3}Al_{0.3}Ti_{1.7}(PO_4)_3$, *J. Power Sources*, 2021, **492**, 229631.
14 M. Lei, S. Fan, Y. Yu, J. Hu, K. Chen, Y. Gu, C. Wu, Y. Zhang and C. Li, NASICON-based solid state Li-Fe-F conversion batteries enabled by multi-interface-compatible sericin protein buffer layer, *Energy Storage Mater.*, 2022, **47**, 551–560.
15 J. Zhu, J. Zhao, Y. Xiang, M. Lin, H. Wang, B. Zheng, H. He, Q. Wu, J. Y. Huang and Y. Yang, Chemomechanical failure mechanism study in NASICON-type $Li_{1.3}Al_{0.3}Ti_{1.7}(PO_4)_3$ solid-state lithium batteries, *Chem. Mater.*, 2020, **32**, 4998–5008.
16 X. Hao, Q. Zhao, S. Su, S. Zhang, J. Ma, L. Shen, Q. Yu, L. Zhao, Y. Liu, F. Kang and Y. B. He, Constructing multifunctional interphase between $Li_{1.4}Al_{0.4}Ti_{1.6}(PO_4)_3$ and Li metal by magnetron sputtering for highly stable solid-state lithium metal batteries, *Adv. Energy Mater.*, 2019, **9**, 1901604.
17 L. Zhu, Y. Wang, Y. Wu, W. Feng, Z. Liu, W. Tang, X. Wang and Y. Xia, Boron Nitride-based release agent coating stabilize $Li_{1.3}Al_{0.3}Ti_{1.7}(PO_4)_3$/Li interface with superior lean-lithium electrochemical performance and thermal stability, *Adv. Funct. Mater.*, 2022, **32**, 2201136.
18 P. Hartmann, T. Leichtweiss, M. R. Busche, M. Schneider, M. Reich, J. Sann, P. Adelhelm and J. Janek, Degradation of NASICON-type materials in contact with lithium metal: formation of mixed conducting interphases (MCI) on solid electrolytes, *J. Phys. Chem. C*, 2013, **117**, 21064–21074.
19 J. Tippens, J. C. Miers, A. Afshar, J. A. Lewis, F. J. Q. Cortes, H. Qiao, T. S. Marchese, C. V. Di Leo, C. Saldana and M. T. McDowell, Visualizing chemomechanical degradation of a solid-state battery electrolyte, *ACS Energy Lett.*, 2019, **4**, 1475–1483.
20 L. Luo, Z. Sun, H. Gao, C. Lan, X. Huang, X. Han, P. Su, Z. Zhang, C. Li, W. Huang, Q. Wei, Q. Zhang, M. S. Wang and S. Chen, Insights into the enhanced interfacial stability enabled by electronic conductor layers in solid-state Li batteries, *Adv. Energy Mater.*, 2023, **13**, 2203517.
21 P. Wu, W. Zhou, X. Su, J. Li, M. Su, X. Zhou, B. W. Sheldon and W. Lu, Recent advances in conduction mechanisms, synthesis methods, and improvement strategies for $Li_{1+x}Al_xTi_{2-x}(PO_4)_3$ solid electrolyte for all-solid-state lithium batteries, *Adv. Energy Mater.*, 2022, **13**, 2203440.
22 L. Luo, F. Zheng, H. Gao, C. Lan, Z. Sun, W. Huang, X. Han, Z. Zhang, P. Su, P. Wang, S. Guo, G. Lin, J. Xu, J. Wang, J. Li, C. Li, Q. Zhang, S. Wu, M. S. Wang and S. Chen, Tuning the electron transport behavior at Li/LATP interface for enhanced cyclability of solid-state Li batteries, *Nano Res.*, 2022, **16**, 1634–1641.
23 Y. Liu, C. Li, B. Li, H. Song, Z. Cheng, M. Chen, P. He and H. Zhou, Germanium thin film protected lithium aluminum germanium phosphate for solid-state Li batteries, *Adv. Energy Mater.*, 2018, **8**, 1702374.
24 Y. Liu, Q. Sun, Y. Zhao, B. Wang, P. Kaghazchi, K. R. Adair, R. Li, C. Zhang, J. Liu, L. Y. Kuo, Y. Hu, T. K. Sham, L. Zhang, R. Yang, S. Lu, X. Song and X. Sun, Stabilizing the interface of NASICON solid electrolyte against Li metal with atomic layer deposition, *ACS Appl. Mater. Interfaces*, 2018, **10**, 31240–31248.
25 L. Wang, L. Wang, Q. Shi, C. Zhong, D. Gong, X. Wang, C. Zhan and G. Liu, In-situ constructed SnO_2 gradient buffer layer as a tight and robust interphase toward Li metal anodes in LATP solid state batteries, *J. Energy Chem.*, 2023, **80**, 89–98.
26 J. Yu, Q. Liu, X. Hu, S. Wang, J. Wu, B. Liang, C. Han, F. Kang and B. Li, Smart construction of multifunctional

$Li_{1.5}Al_{0.5}Ge_{1.5}(PO_4)_3$|Li intermediate interfaces for solid-state batteries, *Energy Storage Mater.*, 2022, **46**, 68–75.

27 Y. L. Liao, J. K. Hu, Z. H. Fu, C. Z. Zhao, Y. Lu, S. Li, S. J. Yang, S. Sun, X. L. Wang, J. Liu, J. Q. Huang and H. Yuan, Integrated interface configuration by in-situ interface chemistry enabling uniform lithium deposition in all-solid-state lithium metal batteries, *J. Energy Chem.*, 2023, **80**, 458–465.

28 Z. Yang, H. Yuan, C. Zhou, Y. Wu, W. Tang, S. Sang and H. Liu, Facile interfacial adhesion enabled LATP-based solid-state lithium metal battery, *Chem. Eng. J.*, 2020, **392**, 123650.

29 Y. Jin, C. Liu, X. Zong, D. Li, M. Fu, S. Tan, Y. Xiong and J. Wei, Interface engineering of $Li_{1.3}Al_{0.3}Ti_{1.7}(PO_4)_3$ ceramic electrolyte via multifunctional interfacial layer for all-solid-state lithium batteries, *J. Power Sources*, 2020, **460**, 228125.

30 J. Y. Liang, X. X. Zeng, X. D. Zhang, T. T. Zuo, M. Yan, Y. X. Yin, J. L. Shi, X. W. Wu, Y. G. Guo and L. J. Wan, Engineering janus interfaces of ceramic electrolyte via distinct functional polymers for stable high-voltage Li-metal batteries, *J. Am. Chem. Soc.*, 2019, **141**, 9165–9169.

31 W. Zhou, S. Wang, Y. Li, S. Xin, A. Manthiram and J. B. Goodenough, Plating a dendrite-free lithium anode with a polymer/ceramic/polymer sandwich electrolyte, *J. Am. Chem. Soc.*, 2016, **138**, 9385–9388.

32 L. Pan, S. Sun, G. Yu, X. X. Liu, S. Feng, W. Zhang, M. Turgunov, Y. Wang and Z. Sun, Stabilizing solid electrolyte/Li interface via polymer-in-salt artificial protection layer for high-rate and stable lithium metal batteries, *Chem. Eng. J.*, 2022, **449**, 137682.

33 Z. Chen, G. T. Kim, J. K. Kim, M. Zarrabeitia, M. Kuenzel, H. P. Liang, D. Geiger, U. Kaiser and S. Passerini, Highly stable quasi-solid-state lithium metal batteries: reinforced $Li_{1.3}Al_{0.3}Ti_{1.7}(PO_4)_3$/Li interface by a protection interlayer, *Adv. Energy Mater.*, 2021, **11**, 2101339.

34 Q. Cheng, A. Li, N. Li, S. Li, A. Zangiabadi, T. D. Li, W. Huang, A. C. Li, T. Jin, Q. Song, W. Xu, N. Ni, H. Zhai, M. Dontigny, K. Zaghib, X. Chuan, D. Su, K. Yan and Y. Yang, Stabilizing solid electrolyte-anode interface in Li-metal batteries by boron nitride-based nanocomposite coating, *Joule*, 2019, **3**, 1510–1522.

35 T. Gu, L. Chen, Y. Huang, J. Ma, P. Shi, J. Biao, M. Liu, W. Lv and Y. He, Engineering ferroelectric interlayer between $Li_{1.3}Al_{0.3}Ti_{1.7}(PO_4)_3$ and lithium metal for stable solid-state batteries operating at room temperature, *Energy Environ. Mater.*, 2022, e12531.

36 M. Ghafari, Z. Sanaee, A. Babaei and S. Mohajerzadeh, Realization of high-performance room temperature solid state Li-metal batteries using a LiF/PVDF-HFP composite membrane for protecting an LATP ceramic electrolyte, *J. Mater. Chem. A*, 2023, **11**, 7605–7616.

37 C. Huang, S. Huang, A. Wang, Z. Liu, D. Pei, J. Hong, S. Hou, L. Vitos and H. Jin, Stabilizing the $Li_{1.4}Al_{0.4}Ti_{1.6}(PO_4)_3$/Li interface with an in situ constructed multifunctional interlayer for high energy density batteries, *J. Mater. Chem. A*, 2022, **10**, 25500–25508.

38 W. Kong, Z. Jiang, Y. Liu, Q. Han, L. X. Ding, S. Wang and H. Wang, Stabilizing $Li_{1.3}Al_{0.}3Ti_{1.7}(PO_4)_3$|Li metal anode interface in solid-state batteries by kevlar aramid nanofiber-based protective coating, *Adv. Funct. Mater.*, 2023, 2306748.

39 C. Yan, X. B. Cheng, Y. X. Yao, X. Shen, B. Q. Li, W. J. Li, R. Zhang, J. Q. Huang, H. Li and Q. Zhang, An armored mixed conductor interphase on a dendrite-free lithium-metal anode, *Adv. Mater.*, 2018, **30**, 1804461.

40 Q. Gao, D. Wu, X. Zhu, P. Lu, T. Ma, M. Yang, L. Chen, H. Li and F. Wu, Dendrite-free lithium-metal all-solid-state batteries by solid-phase passivation, *Nano Energy*, 2023, **117**, 108922.

41 Y. Lu, C. Z. Zhao, H. Yuan, X. B. Cheng, J. Q. Huang and Q. Zhang, Critical current density in solid-state lithium metal batteries: mechanism, influences, and strategies, *Adv. Funct. Mater.*, 2021, **31**, 2009925.

42 Z. Li, S. Zhang, K. Qian, P. Nie, S. Chen, X. Zhang, B. Li, T. Li, G. Wei and F. Kang, Efficient construction of a C_{60} interlayer for mechanically robust, dendrite-free, and ultrastable solid-state batteries, *iScience*, 2020, **23**, 101636.

43 W. Lei, C. Zhang, R. Qiao, M. Ravivarma, H. Chen, F. B. Ajdari, M. Salavati-Niasari and J. Song, Stable Li|LAGP interface enabled by confining solvate ionic liquid in a hyperbranched polyanionic copolymer for NASICON-based solid-state batteries, *ACS Appl. Energy Mater.*, 2023, **6**, 4363–4371.

44 C. Huang, F. Wang, S. Huang, J. Hong, S. Yuan, S. Hou and H. Jin, The electrochemical failure mechanism investigation of $Li_{1+x}Al_xTi_{2-x}(PO_4)_3$ solid-state electrolytes, *J. Mater. Chem. A*, 2023, **11**, 12034–12042.

45 C. Wang, C. Yang, Y. Du, Z. Guo and H. Ye, Spherical lithium deposition enables high Li-utilization rate, low negative/positive ratio, and high energy density in lithium metal batteries, *Adv. Funct. Mater.*, 2023, **33**, 2303427.

46 F. Han, A. S. Westover, J. Yue, X. Fan, F. Wang, M. Chi, D. N. Leonard, N. J. Dudney, H. Wang and C. Wang, High electronic conductivity as the origin of lithium dendrite formation within solid electrolytes, *Nat. Energy*, 2019, **4**, 187–196.

47 Y. Song, L. Yang, W. Zhao, Z. Wang, Y. Zhao, Z. Wang, Q. Zhao, H. Liu and F. Pan, Revealing the short-circuiting mechanism of garnet-based solid-state electrolyte, *Adv. Energy Mater.*, 2019, **9**, 1900671.

48 X. Ji, S. Hou, P. Wang, X. He, N. Piao, J. Chen, X. Fan and C. Wang, Solid-state electrolyte design for lithium dendrite suppression, *Adv. Mater.*, 2020, **32**, 2002741.

49 H. Huo, Y. Chen, R. Li, N. Zhao, J. Luo, J. G. Pereira da Silva, R. Mücke, P. Kaghazchi, X. Guo and X. Sun, Design of a mixed conductive garnet/Li interface for dendrite-free solid lithium metal batteries, *Energy Environ. Sci.*, 2020, **13**, 127–134.